JOURNAL OF COMPUTATIONAL PHYSICS 46, 69–96 (1982)

A Numerical Model for Nonaxisymmetric MHD Instabilities*

A. I. SHESTAKOV, J. KILLEEN, AND D. D. SCHNACK†

National Magnetic Fusion Energy Computer Center, Lawrence Livermore National Laboratory Livermore, California 94550

Received July 31, 1981; revised October 19, 1981

A method is described for studying the stability of two-dimensional equilibria of magnetically confined plasmas. The equations of magnetohydrodynamics (MHD) are linearized and the resulting time-dependent first-order system of equations is solved. Unstable equilibria result in exponentially growing solutions. The plasma is assumed to be incompressible and resistivity is included in the model. The equations are solved in cylindrical coordinates and the perturbations vary as $f_1(r, z, t) \exp(in\theta)$. Nonaxisymmetric modes ($n \neq 0$) are considered. Tearing mode results for one-dimensional analytic equilibria are compared with earlier work. A numerically generated equilibrium, modeling the field reversed theta pinch experiment, is shown to be unstable to the $n = 1$ tilting mode.

1. INTRODUCTION

The generation of energy from fusion via magnetic confinement depends on several factors. The plasma, an ionized gas, is heated to a sufficiently high temperature and needs to be contained by magnetic fields long enough for the fusion reactions to occur.

The magnetically confined plasma may be described by the equations of magnetohydrodynamics (MHD). The complex nonlinear nature of these equations requires that simplifications be made to study different properties. One equation arises in the discussion of equilibria. The solution is assumed to be time independent and usually static. The equation of motion then reduces to force balance; the forces due to the pressures of the plasma treated as a fluid are balanced by those exerted by the magnetic fields. The resulting equation is nonlinear and in most interesting cases is solved numerically. The equilibrium may be unstable, however. Small perturbations about such an equilibrium grow exponentially and in a short time may significantly deform the original configuration, possibly destroying confinement.

The growth of the instability may occur on several time scales. The slowest characteristic time is the resistive diffusion time τ_R which is the time for the equilibrium fields to diffuse away due to collisions of the particles. A significantly faster time is

* Work performed under the auspices of the U. S. Department of Energy by the Lawrence Livermore National Laboratory under contract number W–7405–ENG–48.

† Present address: Los Alamos National Laboratory, Los Alamos, New Mexico 87545.

0021-9991/82/040069–28$02.00/0

the hydromagnetic-transit time τ_H the time required for an Alfvén wave to travel across the plasma. The fastest growing instabilities are those whose growth time is comparable to τ_H. These instabilities are independent of plasma resistivity and can be studied with a simplified set of equations. Other instabilities grow on time scales between τ_R and τ_H. Their study requires use of a higher order system of equations which include resistivity.

The study of resistive instabilities was first investigated by Furth *et al.* [1] who considered a plane-plasma sheet in a sheared magnetic field. The effects of resistivity are confined to a narrow region in which the resistive MHD equations are used. The infinite-conductivity equations are solved outside of this region and the corresponding solutions are matched at the intersection. Killeen [2] solved the full set of incompressible–resistive MHD equations using numerical methods for both Cartesian and cylindrical coordinate systems. Effects of viscosity, compressibility, and thermal conductivity were later introduced by Dibiase and Killeen [3]. In the above studies, the equilibria were given by one-dimensional analytic functions; the walls, when considered, were allowed to come in contact with the plasma.

In this paper we shall present a numerical method to study the stability of two-dimensional axisymmetric equilibria that will in general be generated numerically. We envision plasmas surrounded by vacuum regions. Our approach is to linearize the resistive MHD equations about the equilibrium and solve the resulting equations for the perturbed quantities. These perturbations vary as $f_1(r, z, t) \exp(in\theta)$ and we shall consider $n \geqslant 1$. Axisymmetric instabilities ($n = 0$) are studied with a simplified set of variables [4]. We shall obtain time-dependent equations. Unstable equilibria are characterized by the appearance of an exponentially growing solution which dominates the result.

In Section 2 we shall describe the mathematical model, and in Section 3 the boundary and initial conditions are discussed. Section 4 proves that no spurious solutions arise from our system of equations. The numerical method used to solve the system of equations is described in Section 5. Numerical results are given in Section 6; first earlier results are corroborated in order to demonstrate the ability of our method to study resistive instabilities. Later, a two-dimensional equilibrium modeling an existing experimental device is studied. Last, we shall discuss extensions to other experiments and give concluding remarks. The component equations and other long expressions are found in the appendix.

2. Mathematical Model

We shall assume that the equations of MHD for a single fluid describe the plasma. The normalized equation of motion is,

$$\rho \left[\frac{\partial \mathbf{v}}{\partial t} + (\mathbf{v} \cdot \nabla) \mathbf{v} \right] = (\nabla \times \mathbf{B}) \times \mathbf{B} - \nabla p, \tag{1}$$

where ρ is the density of the fluid, $\mathbf{v}$ the fluid velocity, $\mathbf{B}$ the magnetic induction, and p the fluid pressure. The equation of state is

$$p = \rho T, \tag{2}$$

where T is the temperature. The electromagnetic fields are related via Maxwell's equations. Plasma resistivity, η is included in Ohm's law.

Maxwell's equations and Ohm's law are combined to give a time-dependent equation for $\mathbf{B}$:

$$\frac{\partial \mathbf{B}}{\partial t} = -\frac{1}{S} \nabla \times (\eta \nabla \times \mathbf{B}) + \nabla \times (\mathbf{v} \times \mathbf{B}). \tag{3}$$

We have used two characteristic times, the Alfvén time τ_H and the resistive-diffusion time τ_R in our normalization. In CGS units, $\tau_H \equiv a(4\pi\langle\rho\rangle)^{1/2}/\langle B\rangle$, and $\tau_R \equiv 4\pi a^2/\langle\eta\rangle c^2$. Spatial distances have been normalized to the characteristic distance a; $\langle u\rangle$ denotes a characteristic value of u. Time is normalized to τ_H, velocities to the Alfvén speed a/τ_H and $S(\equiv\tau_R/\tau_H)$ is the magnetic Reynolds number.

The dependent variables are expressed as a sum of equilibrium and perturbed quantities, $f = f_0 + f_1$, respectively. The equilibrium is assumed to be static ($\mathbf{v}_0 = 0$) and the fields $\mathbf{B}_0$ are given functions obtained from solving the pressure balance equation. Equations (1) and (3) are linearized and effects of perturbed resistivity do not appear. Using Eq. (3) the time behavior of the perturbed magnetic field is given by

$$\frac{\partial \mathbf{B}_1}{\partial t} = -\frac{1}{S} \nabla \times (\eta \nabla \times \mathbf{B}_1) + \nabla \times (\mathbf{v}_1 \times \mathbf{B}_0). \tag{4}$$

We assume incompressibility. This and Maxwell's equations imply

$$\nabla \cdot \mathbf{v}_1 = 0 = \nabla \cdot \mathbf{B}_1. \tag{5}$$

We linearize Eq. (1), take the curl twice and neglect the perturbed density. Using Eq. (5), we find

$$-\frac{\partial}{\partial t}(\nabla^2 \mathbf{v}_1) = \nabla \times \nabla \times [(\mathbf{B}_0 \cdot \nabla)\mathbf{B}_1 + (\mathbf{B}_1 \cdot \nabla)\mathbf{B}_0] \tag{6}$$

The principal equations are (4) and (6). We assume that $\mathbf{B}_0$ is the known equilibrium field, and will use several choices for η. The perturbations very as

$$f_1 = f_1(r, z, t) \exp(in\theta). \tag{7}$$

We shall consider nonaxisymmetric modes ($n \neq 0$). By proper orientation the above coordinate system allows us to consider either cylindrical or toroidal geometries. Equations (5), (7) and the assumption $n \neq 0$ allow elimination of the toroidal components of $\mathbf{v}_1$ and $\mathbf{B}_1$. When these substitutions are inserted in Eqs. (4) and (6), we obtain a set of four coupled complex-partial differential equations for the poloidal components: B_{r1}, B_{z1}, v_{r1}, v_{z1}. We write these variables as $f_1(r, z, t) = f_1^R(r, z, t) + i f_1^I(r, z, t)$. This substitution yields eight real equations. In the following we will not write the superscript "R" to denote the real component of the perturbation. The component equations are found in the appendix.

3. Boundary and Initial Conditions

In all cases discussed the domain of interest is rectangular.

$$R_0 \leqslant r \leqslant R_M, \qquad Z_0 \leqslant z \leqslant Z_N. \tag{8}$$

Case 1. We first reproduce results of Dibiase and Killeen [3] for one-dimensional equilibria $\mathbf{B}_0(r)$. This work studied resistive instabilities in cylindrical plasmas, where the perturbations varied as $f_1 = f_1(r, t) \exp(in\theta + ikz)$. In the present work, we model this by setting,

$$R_0 = 0, \qquad R_M > 0, \quad -Z_0 = Z_N = \pi/k.$$

The perturbations are required to be finite at $r = 0$ (see below). We use conducting wall boundary conditions at $r = R_M$, and periodic conditions at $z = \pm Z_N$.

Case 2. Next we study the stability of two-dimensional equilibria without toroidal field, $\mathbf{B}_0 = B_{r0}(r, z)\,\hat{r} + B_{z0}(r, z)\,\hat{z}$. The equilibrium was computed by Anderson and Barnes [5] and models the reversed field theta pinch experiment FRX-B [6] at the Los Alamos National Laboratory. This scenario imposes $R_0 = 0$, $R_M =$ device radius, $-Z_0 = Z_N =$ device half length.

When the domain of computation extends to the z axis (i.e., $0 \leqslant r \leqslant R_M$), the boundary conditions on the axis depend on the toroidal mode number n. We shall use the same conditions as in [3]:

$$\begin{aligned} n = 1 \qquad & \frac{\partial B_{r1}}{\partial r} = \frac{\partial v_{r1}}{\partial r} = 0 = B_{z1} = v_{z1} \qquad \text{at} \quad r = 0 \\ n \geqslant 2 \qquad & B_{r1} = B_{z1} = v_{r1} = v_{z1} = 0 \qquad \text{at} \quad r = 0. \end{aligned} \tag{9}$$

At conducting walls we require that $\mathbf{n} \cdot \mathbf{B}_1 = \mathbf{n} \cdot \mathbf{v}_1 = 0$. Furthermore, requiring that the toroidal component of the perturbed current vanish at the wall gives a Neumann boundary condition for the tangential-magnetic field component. We also need to prescribe the tangential-velocity component at the walls. Here we assume symmetry and likewise obtain a Neumann condition. Thus, when $r = R_W$ defines a conducting wall we set

$$v_{r1} = B_{r1} = 0 = \frac{\partial v_{z1}}{\partial r} = \frac{\partial B_{z1}}{\partial r} \qquad \text{at} \quad r = R_W. \tag{10a}$$

Along walls given by $z = Z_W$,

$$v_{z1} = B_{z1} = 0 = \frac{\partial v_{r1}}{\partial z} = \frac{\partial B_{r1}}{\partial z} = 0. \tag{10b}$$

No distinction in the boundary conditions is made for the real or imaginary components of the modes.

When the equilibrium is unstable the modes grow exponentially in time. Hence, the growth rate and the spatial mode structure is independent of the initial conditions. The calculation proceeds until the fastest growing mode dominates. At the start we shall give the radial velocity an initial smooth profile. Specific initial conditions are described in the results.

4. Physical Validity of Solutions

We shall now show that if $\mathbf{v}_1$ and $\mathbf{B}_1$ are exponentially growing solutions of Eqs. (4) and (6), then these functions represent unstable perturbations of the equilibrium.

Define the vector

$$K_1 \equiv (\nabla \times \mathbf{B}_0) \times \mathbf{B}_1 + (\nabla \times \mathbf{B}_1) \times \mathbf{B}_0 \tag{11}$$

If p is the growth rate (e.g., $\mathbf{v}_1(\mathbf{x}, t) = \mathbf{v}_1(\mathbf{x}) \exp(pt)$), consider the vector

$$\mathbf{Q} \equiv -p\mathbf{v}_1 + \mathbf{K}_1 \tag{12}$$

We will require that

$$\mathbf{Q} \cdot \hat{n} = 0, \tag{13}$$

where $\hat{n}$ is the unit normal to the conducting wall. Since $\hat{n} \cdot \mathbf{v}_1 = 0$, Eq. (13) is satisfied whenever

$$\hat{n} \times (\nabla \times \mathbf{B}_0) = 0 = \hat{n} \times (\nabla \times \mathbf{B}_1). \tag{14}$$

The first relationship holds since the plasma is insulated from the solid walls by a vacuum region where the equilibrium current vanishes. The second half of Eq. (14) has previously been imposed on the poloidal components of $\mathbf{B}_1$ (see Section 3). The requirement for the toroidal component $B_{\theta 1}$ is

$$\partial(rB_{\theta 1})/\partial r = 0 \qquad \text{at} \quad r\text{-walls}$$

and (15)

$$\partial B_{\theta 1}/\partial z = 0 \qquad \text{at} \quad z\text{-walls}.$$

Using div $\mathbf{B}_1 = 0$ to eliminate $B_{\theta 1}$, Eqs. (15) impose additional conditions on the derivatives of B_{r1} and B_{z1}. Details are found in the Appendix (Eqs. (A5) and (A6)). Thus, Eq. (13) holds.

Equations (6) and (12) imply that $\nabla \times (\nabla \times \mathbf{Q}) = 0$. Therefore,

$$\nabla \times \mathbf{Q} = \nabla \phi, \tag{16}$$

where the scalar function ϕ is the solution to the Neumann problem

$$\nabla^2 \phi = 0. \tag{17}$$

Boundary conditions for Eq. (17) are obtained by prescribing

$$\frac{\partial \phi}{\partial n} = \hat{n} \cdot (\nabla \times \mathbf{Q}) = 0. \tag{18}$$

In the Appendix we shall show what additional conditions on $\mathbf{B}_1$ are required to satisfy Eq. (18). Let s_0 be a point on the boundary and impose $\phi(s_0) = 0$. The function ϕ is now uniquely determined and given by $\phi \equiv 0$. Recalling Eq. (16), it follows that $\mathbf{Q}$ is curl free, hence, $\mathbf{Q}$ is the gradient of a scalar function,

$$Q = \nabla p_1. \tag{19}$$

This function is computed by solving the elliptic problem,

$$\nabla^2 p_1 = \nabla \cdot \mathbf{Q} = \nabla \cdot \mathbf{K}_1. \tag{20}$$

The boundary condition for Eq. (20) is given by Eq. (13), i.e., $\partial p_1/\partial n = 0$.

The function p_1 is identified as the perturbed pressure. Equations (12) and (19) imply that

$$p\mathbf{v}_1 = -\nabla p_1 + \mathbf{K}_1. \tag{21}$$

As asserted, the modes $\mathbf{v}_1$ and $\mathbf{B}_1$ satisfy the linearized equation of motion; thereby constituting perturbations of the equilibrium $\mathbf{B}_0$.

5. Method of Solution

The system of interest can be summarized by the following equations (see Eqs. (A1)–(A4), for full details):

$$\frac{\partial B_{r1}}{\partial t} = \frac{\eta}{S}\left[M(B_{r1}) + \frac{2}{r}\frac{\partial B_{z1}}{\partial z}\right] + \frac{1}{S}\frac{\partial \eta}{\partial z} j_{\theta 1} + F_1(v_{r1}, v_{z1}) - nB_{\theta 0}\frac{v_{r1}^I}{r}, \tag{22}$$

$$\frac{\partial B_{z1}}{\partial t} = \frac{\eta}{S} L(B_{z1}) - \frac{1}{S}\frac{\partial \eta}{\partial r} j_{\theta 1} + F_2(v_{r1}, v_{z1}) - nB_{\theta 0}\frac{v_{z1}^I}{r}, \tag{23}$$

$$\frac{\partial}{\partial t} L(v_{z1}) = F_3(B_{r1}, B_{z1}, B^I_{r1}, B^I_{z1}), \tag{24}$$

$$\frac{\partial}{\partial t}\left[M(v_{r1}) + \frac{2}{r}\frac{\partial v_{z1}}{\partial z}\right] = F_4(B_{r1}, B_{z1}, B^I_{r1}, B^I_{z1}), \tag{25}$$

where

$$j_{\theta 1} \equiv \frac{\partial B_{r1}}{\partial z} - \frac{\partial B_{z1}}{\partial r}, \tag{26}$$

$$L(u) \equiv \frac{1}{r}\frac{\partial}{\partial r}\left(r\frac{\partial u}{\partial r}\right) + \frac{\partial^2 u}{\partial z^2} - \frac{n^2}{r^2} u, \tag{27}$$

$$M(u) \equiv L(u) + \frac{2}{r}\frac{\partial u}{\partial r} + \frac{u}{r^2}. \tag{28}$$

The functions F_1, F_2 represent the respective components of $\nabla \times (\mathbf{v}_1 \times \mathbf{B}_0)$ in Eq. (4) and contain derivatives up to first order. The functions F_3, F_4 in Eqs. (24) and (25) denote the components of the r.h.s. of Eq. (6); these functions contain derivatives up to third order in both $\mathbf{B}_0$ and $\mathbf{B}_1$.

Equations for the imaginary components are similar. They are obtained from Eqs. (22)–(25) by substituting u^I for u, and $-u$ for u^I. Thus, the B^I_{z1} equation is

$$\frac{\partial B^I_{z1}}{\partial t} = \frac{\eta}{S} L(B^I_{z1}) + \cdots + nB_{\theta 0}\frac{v_{z1}}{r}. \tag{29}$$

The case with no toroidal field, i.e., $B_{\theta 0} \equiv 0$ is attractive since the real and imaginary component equations decouple and are equivalent. This allows us to solve for only the four real components, B_{r1}, B_{z1}, v_{r1}, and $v_{\theta 1}$.

The elliptic solver used to advance Eqs. (24) and (25) imposes a uniform mesh in z; the r-mesh may be nonuniform. Derivatives are approximated by central differences, e.g.,

$$\frac{\partial u(r_i, z_j)}{\partial r} \sim \frac{u_{i+1,j} - u_{i-1,j}}{r_{i+1} - r_{i-1}}$$

and (30)

$$\frac{\partial^2 u(r_i, z_j)}{\partial r^2} \sim 2\left(\frac{u_{i+1,j} - u_{i,j}}{r_{i+1} - r_i} - \frac{u_{i,j} - u_{i-1,j}}{r_i - r_{i-1}}\right)\Big/(r_{i+1} - r_{i-1}),$$

where u_{ij} denotes the approximation to $u(r_i, z_j)$. These differences are valid for nonuniform meshes, but then become first-order correct.

We use two time-advancement techniques. Version A, an early development, was used whenever the resistivity was held constant or varied only in r and its gradients could be neglected. Such a case arises in stability studies for an equilibrium with little axial variation. An example is the reversed field theta pinch to be described in the next section. Version B is more general; it allows $\eta = \eta(r, z)$, and includes resistivity gradients. We shall first describe Version A.

If the $\nabla\eta$ terms are neglected in Eqs. (22) and (23), note that Eq. (23) does not depend on B_{r1}. Let u^n denote the approximation to u at time $n\Delta t$. Assume that $\mathbf{B}_1^n$, $\mathbf{v}_1^n$ and $\mathbf{B}_1^{n-1}$ are known. Let L_d and F_{d2}, respectfully, denote the finite-difference approximations to the operators L and F_2 found in Eqs. (23) and (27). We first advance B_{z1} by the following scheme:

$$(B_{z1}^{n+1} - B_{z1}^{n-1})/2\Delta t = \frac{\eta}{2S}\,[L_d(B_{z1}^{n+1}) + L_d(B_z^{n-1})] + F_{d2}(v_{r1}^n, v_{z1}^n) - \frac{n}{r} B_{\theta 0} v_{z1}^{I,n}. \tag{31}$$

After solving Eq. (31), the result is used in the difference approximation to Eq. (22)

$$(B_{r1}^{n+1} - B_{r1}^{n-1})/2\Delta t = \frac{\eta}{2S}\,[M_d(B_{r1}^{n+1}) + M_d(B_{r1}^{n-1}) + \frac{2}{r}(D_z B_{z1}^{n+1} + D_z B_{z1}^{n-1})] + F_{d1}(v_{r1}^n, v_{z1}^n) - \frac{n}{r} B_{\theta 0} v_{r1}^{I,n}, \tag{32}$$

where M_d, D_z, and F_{d1} are, respectively, the finite-difference approximations to M in Eq. (28), $\partial/\partial z$ and F_1 in Eq. (22).

The solutions of Eqs. (31) and (32) require the inversion of the operators $(I - (\Delta t\,\eta/S)\,L_d)$ and $(I - (\Delta t\,\eta/S)\,M_d)$. This is easily done when the domain is rectangular, the z-mesh uniform and the number of z-mesh points is of the form 2^p [7]. The last restriction may be relaxed [8], but relaxation of the first two is related to the difficult problem of finding a fast solution to an elliptic equation in an arbitrary domain.

Once, Eqs. (31) and (32) are solved successively, the new fields $\mathbf{B}_1^{n+1}$ are substituted in the time-centered difference approximation to Eqs. (24) and (25)

$$L_d(v_{z1}^{n+1}) - L_d(v_{z1}^n) = \Delta t\, F_{d3}^{n+1/2}(B_{r1}, B_{z1}, B_{r1}^I, B_{z1}^I), \tag{33}$$

and

$$M_d(v_{r1}^{n+1}) - M_d(v_{r1}^n) = \frac{2}{r} D_z(v_{z1}^n - v_{z1}^{n+1}) + \Delta t\, F_{d4}^{n+1/2}(B_{r1}, B_{z1}, B_{r1}^I, B_{z1}^I) \tag{34}$$

where $F_{d3}^{n+1/2}$ and $F_{d4}^{n+1/2}$ are time-centered difference operators, e.g.,

$$F_{d3}^{n+1/2}(B_{r1},\ldots) = F_{d3}((B_{r1}^{n+1} + B_{r1}^n)/2,\ldots).$$

Equation (33) is first solved for v_{z1}^{n+1} and the result is substituted in Eq. (34) to compute v_{r1}^{n+1}. The solution of Eqs. (33) and (34) require inverting large-sparse matrices. This is similarly accomplished by the method described in [7].

The above scheme can be iterated to achieve second-order temporal accuracy. Once Eqs. (33) and (34) are solved, new time-centered velocities are computed, $\mathbf{v}_1^{n+1/2} \equiv (\mathbf{v}_1^n + \mathbf{v}_1^{n+1})/2$. Equations (31) and (32) are modified; $2\Delta t$ is replaced by Δt and $\mathbf{B}_1^{n-1}$ by $\mathbf{B}_1^n$. The result is a time-centered equation for the corrected values $\mathbf{B}_1^{n+1}$. These values are then substituted in Eqs. (33) and (34); the cycle is repeated until a desired accuracy is obtained. Numerical experience has shown that the correction cycles are unnecessary.

The more general Version B is used for configurations in which the plasma is surrounded by a vacuum. In this case the equilibrium resistivity, η, is allowed to increase to a large value. The vacuum is modeled as a highly resistive region. Version B is also used whenever we seek perturbations driven by resistivity gradients.

We shall now describe Version B. The spatial derivatives of $\mathbf{B}_1$ in Eqs. (22) and (23) are separated into those with respect to r and z. The two equations are expressed in vector form as

$$\frac{\partial \mathbf{B}_1}{\partial t} = \frac{1}{S} [\mathbf{d}_r(\mathbf{B}_1) + \mathbf{d}_z(\mathbf{B}_1) + \mathbf{H}(\mathbf{B}_1)] + \mathbf{F}(\mathbf{v}_1), \tag{35}$$

where $\mathbf{d}_i$ contains derivatives in the i-direction, $\mathbf{H}$ collects the nondifferented terms and $\mathbf{B}_1 = (B_{r1}, B_{z1})^{\mathrm{T}}$. A similar equation holds for $\mathbf{B}_1^l$. Let $\mathbf{D}_i$ and $\mathbf{F}_d$ denote the finite-difference approximations to the operators $\boldsymbol{d}_i$ and $\mathbf{F}$ in Eq. (35); assume that $\mathbf{B}_1^n$, $\mathbf{v}_1^n$ are known. Equation (35) is discretized using an alternating direction-implicit scheme (ADI)

$$\begin{aligned}(\mathbf{B}_1^{n+1/2} - \mathbf{B}_1^n)/(\Delta t/2) = S^{-1}[&\mathbf{D}_r(\mathbf{B}_1^{n+1/2}) + \mathbf{D}_z(\mathbf{B}_1^n) + \tfrac{1}{2}\mathbf{H}(\mathbf{B}_1^{n+1/2} + \mathbf{B}_1^n)] \\ &+ \mathbf{F}_d(\mathbf{v}_1^n),\end{aligned} \tag{36a}$$

$$\begin{aligned}(\mathbf{B}_1^{n+1} - \mathbf{B}_1^{n+1/2})/(\Delta t/2) = S^{-1}[&\mathbf{D}_r(\mathbf{B}_1^{n+1/2}) + \mathbf{D}_z(\mathbf{B}_1^{n+1}) \\ &+ \tfrac{1}{2}\mathbf{H}(\mathbf{B}_1^{n+1} + \mathbf{B}_1^{n+1/2})] + \mathbf{F}_d(\mathbf{v}_1^n).\end{aligned} \tag{36b}$$

The velocity terms $\mathbf{F}_d(\mathbf{v}_1^n)$ are left explicit. These equations lead to linear systems in block-tridiagonal form. The coefficients of the system are time independent, hence, the L–U decomposition of the matrices is done only once. By properly arranging the back-substitution steps, the innermost DO-LOOPS can be vectorized [9].

Once Eq. (36b) is solved for $\mathbf{B}_1^{n+1}$, the velocity fields are advanced using Eqs. (33) and (34). As in Version A, this scheme may be iterated. The newly computed $\mathbf{v}_1^{n+1}$ are used to define a time-centered velocity $\mathbf{v}_1^{n+1/2} = (\mathbf{v}_1^{n+1} + \mathbf{v}_1^n)/2$. This field is then substituted into Eqs. (36a) and (36b), giving a system of equations for the corrected values $\mathbf{B}_1^{n+1}$. Corrected values for $\mathbf{v}_1^{n+1}$ are computed as in Version A.

6. Numerical Results

We shall investigate the stability of several equilibria. The problem consists of prescribing the boundary and initial conditions for the perturbations $\mathbf{B}_1$ and $\mathbf{v}_1$ and specifying the equilibrium of interest $\mathbf{B}_0$. If the equilibrium is unstable, the equations yield exponentially growing solutions, $f = f_1(r, z)\, e^{pt}$, where p is the growth rate. We compute a pointwise growth rate $p_{ij} = (2/\Delta t)(f_{ij}^{n+1} - f_{ij}^{n})/(f_{ij}^{n+1} + f_{ij}^{n})$. When the modes have settled into exponential growth and p_{ij} approaches a constant over the entire mesh for every component at every time level, the computation is terminated. A slight modification of the above can be used to diagnose growth rates with complex p [10]. We have not observed this behavior in our studies.

6.1. *One-Dimensional Equilibria Studies*

First we shall present results that corroborate earlier simpler models ([3, 11]). These one-dimensional equilibria $\mathbf{B}_0 = \mathbf{B}_0(r)$ are given in terms of analytic functions. The plasma is cylindrical and infinite in length and extends radially outward to a conducting wall. In the cylindrical coordinate system used, z defines the axial length and θ the azimuthal angle. Dibiase and Killeen assume that the modes vary as $f_1(r, t)$ $\exp(in\theta + ikz)$; and perform a parameter study of n and k.

The work of Dibiase and Killeen is one dimensional. Once k and n are fixed, linear-difference equations are solved for the one-dimensional variables. We shall reproduce those results by specifying n, and define the domain, $0 \leqslant r \leqslant R_W$, $|z| \leqslant \pi/k$. At time $t = 0$, the radial components of $\mathbf{v}_1$ have a trigonometric axial dependence, e.g., $v_{r1} = v_{r1}(r) \cos kz$, $v_{r1}^I = v_{r1}(r) \sin kz$. The radial profile depends on n,

$$\begin{aligned} v_{r1}(r) &= (1 - r/R_\omega)^2, && \text{if} \quad n = 1, \\ &= r(1 - r/R_\omega)^2, && \text{if} \quad n > 1 \quad \text{at} \quad t = 0. \end{aligned} \tag{37}$$

Although the final radial structure is determined by the case chosen and agrees with the work of [3, 11], the axial-trigonometric variation remains unchanged. In this study, periodic boundary conditions are imposed in the z-direction.

Occasionally the trigonometric structure in z is destroyed; higher harmonics are introduced into the calculation by the difference scheme. We control these in one of two ways. For the 1-D models "filtering" may be used. After each time step discrete Fourier analysis is done in the z-direction and only the longest $2\pi/k$ wavelength is allowed to remain. Another technique is "smoothing" [12]: if $u_{i,j}^{n+1,*}$ denotes the result of the time advancement, the "smoothed"

$$u_{i,j}^{n+1} = (1 - 2w\Delta t)\, u_{i,j}^{n+1,*} + w\Delta t(u_{i,j-1}^{n+1,*} + u_{i,j+1}^{n+1,*}) \tag{38}$$

and defines the approximation to $u(r_i, z_j)$ at time $(n+1)\Delta t$. Care must be exercised when using smoothing as it dampens the growth of all the wavelengths [13], albeit the shorter wavelengths are suppressed more than the longer ones. The "amplification factor" is $1 - 4w\Delta t \sin^2(\pi j/N)$, where $j = 1, 2, \ldots, N/2$; longer wavelengths corresponding to smaller values of j. In order to avoid overdamping it is required that $0 \leqslant w\Delta t \leqslant \frac{1}{4}$. For small $w\Delta t$, smoothing diminishes the growth of the longest wavelength by $\exp(-4w\Delta t(\pi/N)^2)$ in one time step. If the solution is to grow by a factor $\exp(p\Delta t)$, the effect of smoothing is to produce a smaller growth rate. One then needs to compare the resulting numerical growth rate with $4w(\pi/N)^2$. We used smoothing only in the z-direction and only on the velocity components. It is noteworthy to mention that for the $1-D$ equilibria models discussed here, the $\exp(ikz)$ structure of the perturbations is maintained.

Before comparing our results with those of [3, 11], we note a difference in the two normalizations. Our time variable is normalized to the Alfvén time, τ_H, while the earlier work normalized to the resistive-diffusion time, τ_R. Since $S = \tau_R/\tau_H$, the growth rates need to be scaled properly. If p_A, p_R, respectfully, denote the growth rates of the present work and that of Dibiase and Killeen, the scaling algorithm is $p_A = p_R/S$.

In order to observe the effects of resistivity in a reversed field configuration, we consider the Lundquist fields [14] or the Bessel Function Model (BFM). Similar configurations can be constructed in the laboratory. The BFM is an example of a

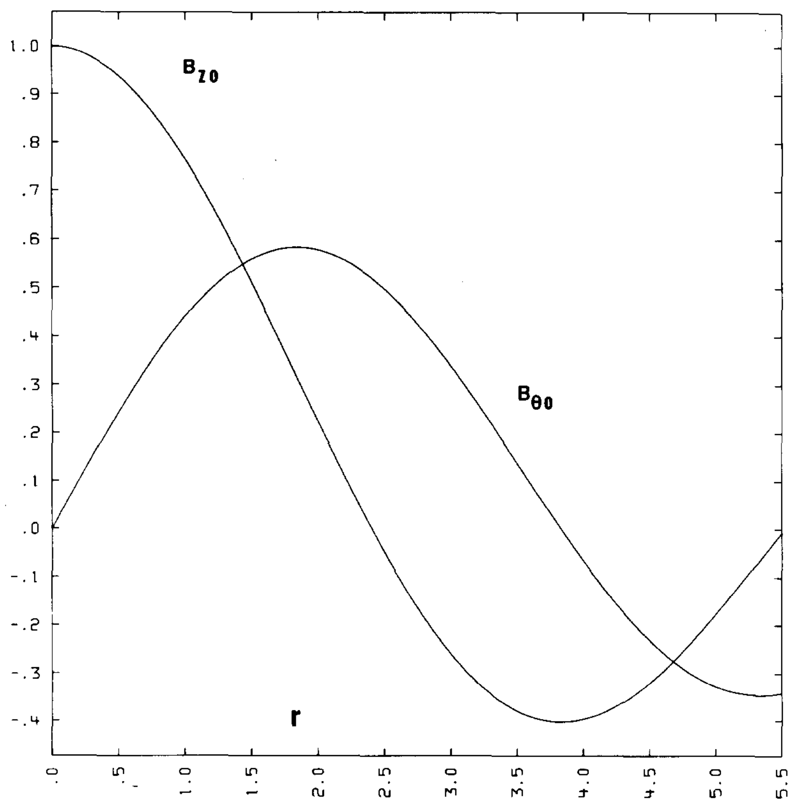

FIG. 1. Bessel Function Model profiles.

force-free configuration. The equilibrium current $\sim\nabla \times \mathbf{B}_0 = \nu\mathbf{B}_0$, therefore, $\nabla p_0 = 0$. Such a configuration is given by

$$\mathbf{B}_0 = J_1(r)\,\hat{\theta} + J_0(r)\,\hat{z}, \tag{39}$$

where J_0 and J_1 are Bessel functions of the first kind. The profiles are shown in Fig. 1; the field is sheared and has a reversed axial component. In order to have a realistic configuration, only one B_{z0} sign reversal is allowed, hence, the wall radius $R_W < 5.520$.

For this model we fix $R_W = 5.5$ thereby getting a configuration unstable to tearing modes. Fig. 2 displays a parameter study of the growth rate p vs. k for $S = 100$, $n = 1$. We present both our results as well as those of Dibiase. (For comparison purposes, the second results have been rescaled.) Figure 3 is a radial profile of the v components for $S = 100$, $n = 1$, $k = 0.3$. This figure is contrasted with Fig. 4, where we show the same profiles for $S = 10^4$. The steepening of the profiles for larger S is characteristic of tearing modes indicating a narrowing singular surface. The results for the larger S were obtained using 32 uniformly distributed axial points, and 140 radial points. The radial mesh was not uniform allowing a finer resolution of the large gradients. Figure 5 plots the variation of p, the growth rate, with S. We also show a linear least-squares fit to the logarithm of the relationship: $p = \alpha S^{\beta}$, and the resulting interpolant to the largest two values of S, 4000 and 10,000. The respective exponents are $\beta = -0.453$ and $\beta -0.558$. These results are in excellent qualitative agreement to numerical calculations for the sheet pinch equilibrium model [15]. The growth rate for smaller S is less than that predicted by analysis. The analytic theory of Furth *et al.* [1] predict $\beta = -0.6$ (when time is normalized to τ_H). We note that the theory holds only for asymptotically increasing S. At lower values, the parabolic terms in Eq. (14) are expected to introduce greater diffusion thereby decreasing the growth rate.

The results show that our model correctly computes resistive MHD modes. The

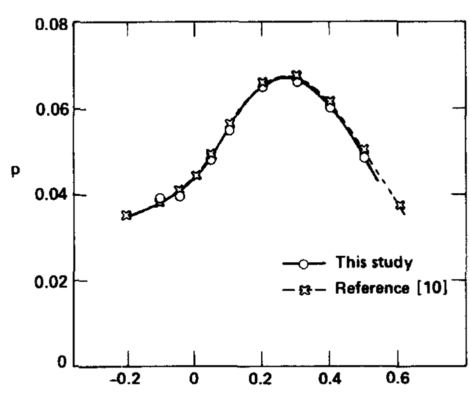

FIG. 2. Bessel Function Model. Growth rate p vs. axial wave number k; $n = 1$, $S = 100$.

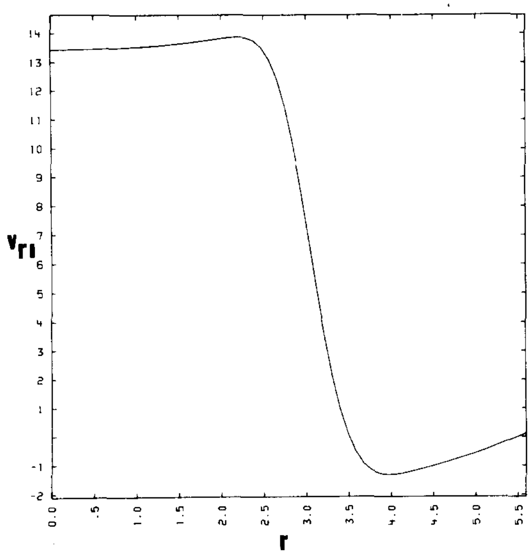

FIG. 3a. Bessel Function Model. Perturbed v_{r1}; $S = 100$, $n = 1$, $k = 0.3$.

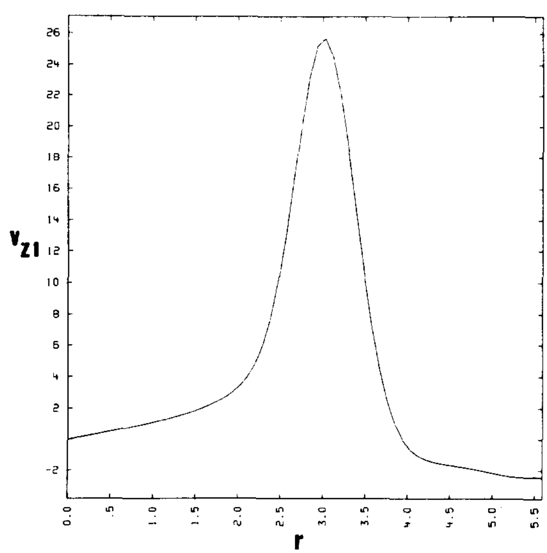

FIG. 3b. Bessel Function Model. Perturbed v_{z1}; $S = 100$, $n = 1$, $k = 0.3$.

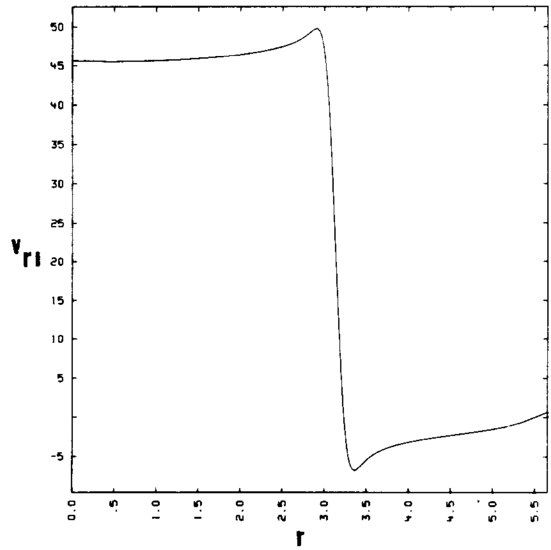

FIG. 4a. Bessel Function Model. Perturbed v_{r1}; $S = 10^4$, $n = 1$, $k = 0.3$.

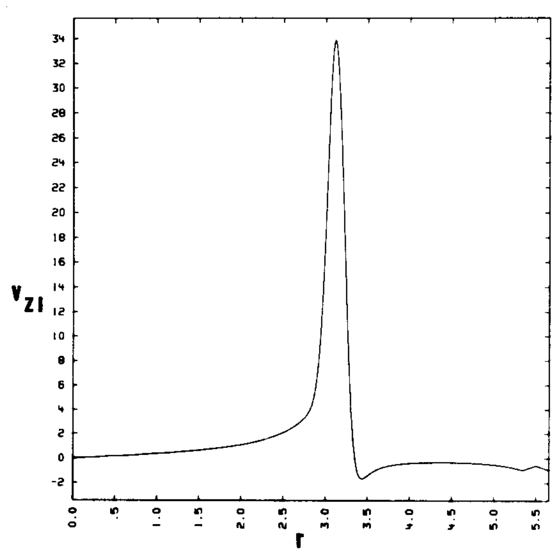

FIG. 4b. Bessel Function Model. Perturbed v_{z1}; $S = 10^4$, $n = 1$, $k = 0.3$.

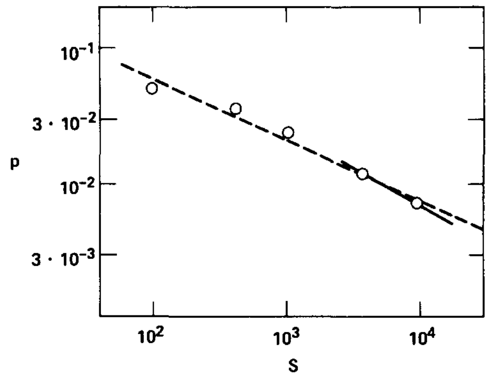

FIG. 5. Bessel Function Model. Growth rate p vs. Magnetic Reynolds number S; $n=1$, $k=0.3$. $p=(0.479)\ S^{(-0.453)}$(---); $p=(1.18)\ s^{(-0.558)}$(—).

proper scaling of p vs. S is demonstrated in Fig. 5, and the narrowing resistive layer is demonstrated by comparing Figs. 3 and 4.

The above simulate tearing instabilities in a diffuse-pinch geometry. One can also construct 1-dimensional equilibria modeling Tokamak discharges. In this case, we approximate large aspect ratios, the axial coordinate, is the toroidal direction, while θ denotes the poloidal angle. We consider the Peaked Tokamak Model studied by Furth *et al.* [16] and by Dibiase [11]. For this model we likewise find different unstable parameter regimes for differing poloidal mode number.

The equilibrium is given in terms of the poloidal field,

$$B_{\theta 0}=r/(1+r^2). \tag{40}$$

We consider the force-free case ($dp_0/dr=0$) by allowing a small variation in B_{z0}. We specify $B_{z0}=7$ at the magnetic axis. This gives a current distribution peaked at $r=0$. The wall position is fixed at $r=2$.

The peaked model is noteworthy for possessing instability regimes in (k, n) space. We make a parameter study for $S=100$, by varying both k and n. In Fig. 6, we plot the dependence of the growth rate vs. k for several values of n. As discussed in [1], a tearing instability develops at the singular point r_s for which:

$$\mathbf{k}\cdot\mathbf{B}_0(r_s)=\frac{n}{r_s}B_{\theta 0}(r_s)+kB_{z0}(r_s)=0. \tag{41}$$

We seek tearing modes by making a judicious choice for k and n. Figure 7 contains the plots of the radial components of $\mathbf{v}_1$ and $\mathbf{B}_1$. The dependence of the growth rate on S is graphed in Fig. 8. The results were obtained after comparing runs with different mesh sizes.

As noted by Dibiase [11], the results do not exhibit the typical behavior of tearing modes. Both the growth rate and the mode structure become independent of S,

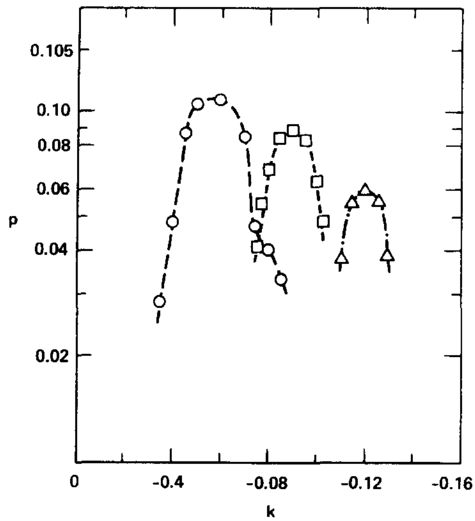

FIG. 6. Peaked Tokamak Model. Growth rate p vs. k; $S = 100$. $n = 1$ (-○-); $n = 2$ (-□-); $n = 3$ (-△-).

characteristic of ideal modes. In Fig. 9 we display the B_{r1} profiles for widely different Reynolds numbers, $S = 10^3$, 10^6.

The computer program computes the fastest growing mode, ideal or resistive. The Peaked Tokamak Model is unstable to the $n = 1$ infinite-conductivity kink mode [16]. For $n = 2$, our results show that the model is likewise unstable to ideal modes. At large the S, the perturbed B_{r1} vanishes at the singular surface (see Fig. 9b), evidence of ideal modes [16]. Our conclusion is that the dominant $n = 2$ instability at large S is an ideal kink mode. At lower values of S, resistivity effects modify both the mode structure and the growth rate.

6.2. *Two-Dimensional Equilibrium Study*

The previous models used analytic functions to approximate one-dimensional equilibria. Our next results simulate a realistic experiment exhibiting the generality of the numerical method. The device is the reversed field theta pinch, FRX-B, at the Los Alamos National Laboratory. The experiment consists of a cylindrical vacuum vessel open at the ends. Relevant parameters are found in Table I.

The calculation of the numerical equilibrium was performed by Anderson and Barnes [5] and is based on the following: The inertial terms in the momentum equation are neglected giving the pressure balance equation (CGS units):

$$4\pi\nabla p_0 = (\nabla \times \mathbf{B}_0) \times \mathbf{B}_0 \tag{42}$$

The axisymmetric fields are given in terms of the flux function,

$$\mathbf{B}_0 = -(\nabla\psi \times \hat{\theta})/r. \tag{43}$$

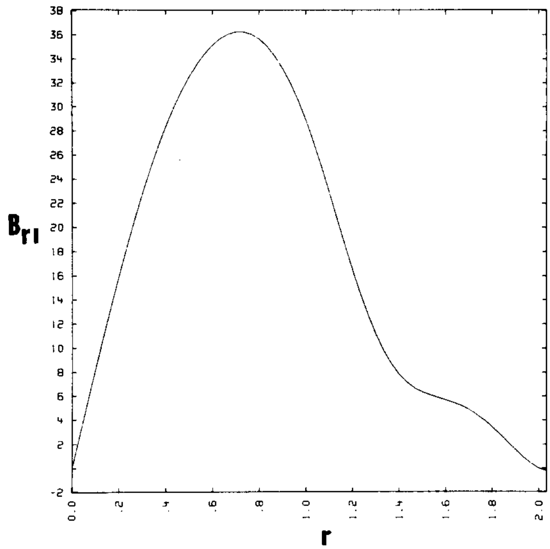

FIG. 7a. Peaked Tokamak Model. Perturbed B_{r1}; $S = 100$, $n = 2$, $k = -0.1$.

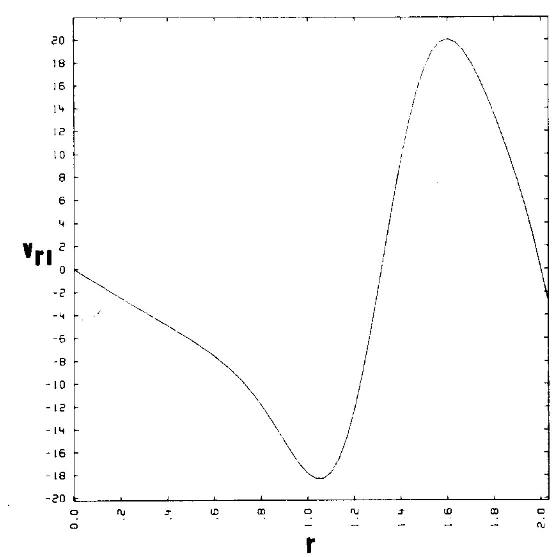

FIG. 7b. Peaked Tokamak Model. Perturbed v_{r1}; $S = 100$, $n = 2$, $k = -0.1$.

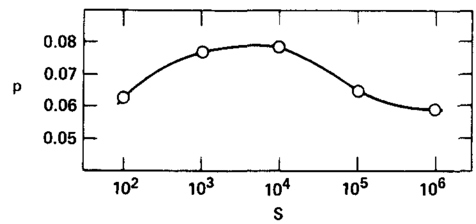

FIG. 8. Peaked Tokamak Model. Growth rate p vs. magnetic Reynolds number S; $n = 2$, $k = -0.1$, $R_w = 2$.

The field does not have a toroidal component, a characteristic of theta pinches. Equation (42) implies that surfaces of constant pressure are tangent to the magnetic surfaces given by $\psi = \text{constant}$. The vector equation (42) is thereby reduced to the single, scalar, usually nonlinear Grad–Shafranov equation

$$\Delta^*\psi = r\frac{\partial}{\partial r}\left(\frac{1}{r}\frac{\partial\psi}{\partial r}\right) + \frac{\partial^2\psi}{\partial z^2} = 4\pi r^2\frac{dp}{d\psi}. \tag{44}$$

The nonlinearity of the equation stems from the choice made for $p(\psi)$, the equilibrium pressure. The toroidal current is proportional to $rp'(\psi)$. Solutions of Eq. (44) have been discussed elsewhere; see McNamara [17] for a good review article. The equilibrium fields and currents can be constructed from the two-dimensional function $\psi(r, z)$ and the one-dimensional $p'(\psi)$.

The perturbation equations require the calculation of derivatives of the equilibrium quantities (see Appendix). These are supplied by a spline package [18]. The function ψ is approximated with bicubic splines and the fields are obtained by differentiating the spline. The two-dimensional current and pressure functions are constructed from their one dimensional $rp'(\psi)$ and $p(\psi)$ formulation. The spline representation allows the evaluation of the required equilibrium quantities; ψ_0, $\mathbf{B}_0$, $j_{\theta 0}$, and p_0, on a grid different from the one used by the equilibrium calculation. Finally, the remaining higher order derivatives of $\mathbf{B}_0$ and $j_{\theta 0}$ are computed using divided differences.

TABLE I

Plasma Parameters for reversed field theta pinch experiment, FRX–B, at LANL

Half length of device	$Z_{MAX} = 45$ cm
Radius of device	$R_w = 12.5$ cm
Separatrix intersection	$z_{sep} = 20.9$ cm
Number density	$n \simeq 10^{16}$ cm^{-3}
Characteristic field strength	$B_{z0}(\text{WALL}) = 8.8$ kg
Temperature	$T \simeq 100$ ev
Magnetic Reynolds number	$S \simeq 10^3$

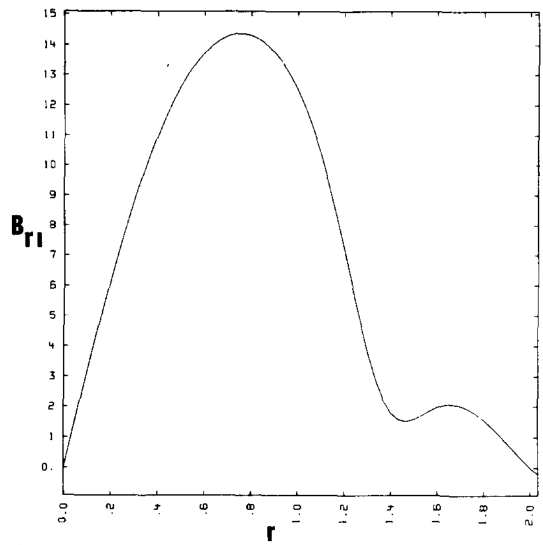

FIG. 9a. Peaked Tokamak Model. Perturbed B_{r1}; $S = 10^3$, $n = 2$, $k = -0.1$.

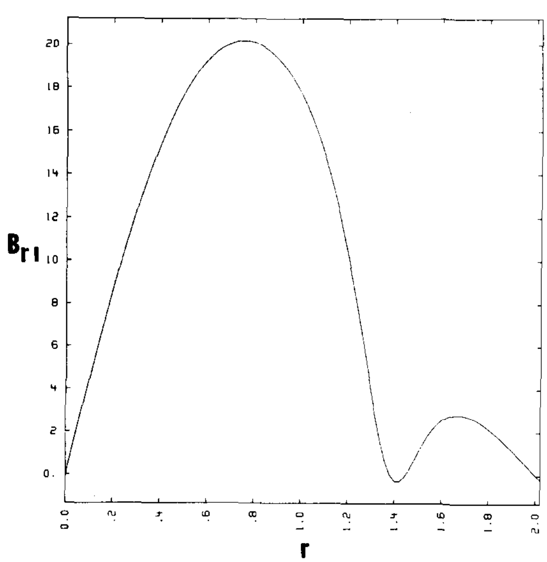

FIG. 9b. Peaked Tokamak Model. Perturbed B_{r1}; $S = 10^6$, $n = 2$, $k = -0.1$.

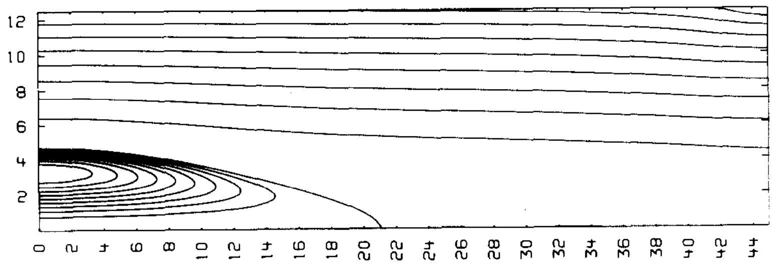

FIG. 10. Flux function contours of FRX–B.

The equilibrium plasma is cylindrical with tapered ends. In Fig. 10 we show the magnetic surface contours; the field is reversed inside the separatrix. The separatrix intersects the r and z axes at ~4.7 and ~21 cm, respectively, making a prolate configuration.

The plasma extends to the region of open-field lines. This is evident from Fig. 11 in which the pressure contours are plotted. The last contour intersects the r axis at 6.2 cm; the vacuum region beyond satisfies $p_0 = j_{\theta 0} = 0$.

Our model solves the same equation throughout the domain of interest. The vacuum is defined to be a highly resistive region. In the results below we set the resistivity to be a step function,

$$\begin{aligned} \eta &= 1, \qquad r < r_\eta, \\ &= X_\eta, \qquad r \geqslant r_\eta, \end{aligned} \tag{45}$$

where $p_0(r, z) = 0$ for $r > r_\eta$. Typical values are $X_\eta \geqslant 10^5$, $r_\eta \geqslant 6.6$ cm. In this way we model the correct vacuum equation: $\nabla \times \mathbf{B}_1 = 0$, by assigning a disproportionally greater influence to the diffusion term in Eq. (4). In order to obtain maximum resolution in the important region containing the plasma, we use a variable radial mesh which becomes coarser in the vacuum. Most of the results were done with Version A, but selected runs were corroborated by Version B.

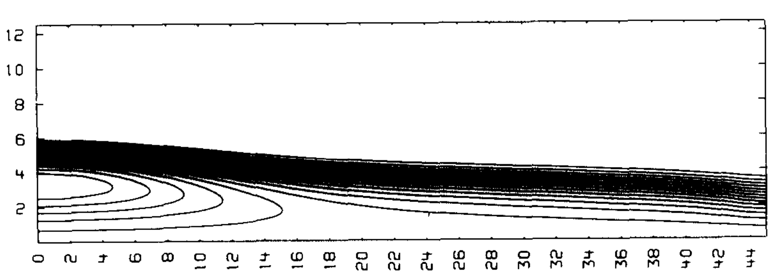

FIG. 11. Equilibrium pressure contours of FRX–B.

The above equilibrium has $B_{\theta 0} = 0$, greatly simplifying the calculation by removing the interdependence between the real and imaginary components of the perturbations. The system decouples into two identical systems of four equations. We, therefore, solve only one system. If the poloidal components vary as $f(r, z) \cos n\theta$, the toroidal ones $B_{\theta 1}, v_{\theta 1}$ necessarily vary as $g(r, z) \sin n\theta$ in order to satisfy Eq. (5).

The calculation is begun by initializing the radial-velocity component. The radial structure depends on the mode number. The axial dependence of the initial conditions is chosen to include both odd and even functions. Furthermore, nonzero values in the vacuum are eliminated by multiplication by the equilibrium pressure, p_0. Thus,

$$v_{r1}(t=0) = v_{r1}(r)\, p(r, z)[\alpha \cos(\pi z/Z_N) + (1-\alpha) \sin(\pi z/Z_N)],$$

where $v_{r1}(r)$ is given by Eq. (37) and $0 \leqslant \alpha \leqslant 1$.

We shall study the equilibrium by varying S and toroidal mode number n. In Fig. 12 we plot the normalized growth rates and note that all three mode numbers studied are unstable. The growth rate is independent of S for $S \gtrsim 10^3$, a sign of ideal [illegible] normalized growth rate of 0.5 is translated into a mode e-folding time of $\sim 1.8\ \mu$secs, also characteristic of ideal modes. The numerical results were obtained by varying all relevant parameters including the mesh size. We note that a too-coarse mesh underestimates the growth rate.

The results for $n = 1$ are interesting. According to the boundary conditions, Eq. (9), this mode is the only one which allows plasma displacement on the axis. The superposition of $\mathbf{B}_1$ on the equilibrium $\mathbf{B}_0$ along $r = 0$ led to the name "tilting mode" since it results in a tilt of the magnetic axis inside the separatrix. We show this in Fig. 13, where we display the field $\mathbf{B}_0 + \varepsilon \mathbf{B}_1$ after both fields have been normalized, e.g., $\mathbf{B}_0$ (normalized) $= \mathbf{B}/\|B_0\|_{\text{MAX}}$. A careful examination shows how the resulting field has been deformed along $r = 0$. The poloidal velocity is shown in Fig. 14.

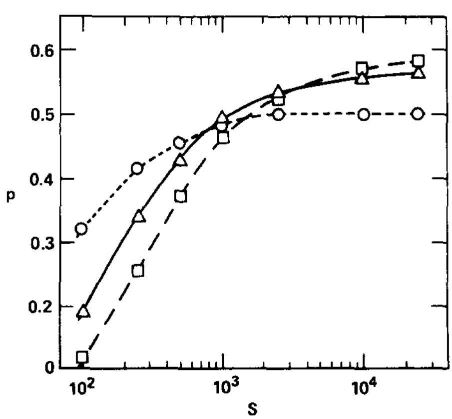

FIG. 12. Stability study of FRX–B. Equilibrium growth rate p vs. magnetic-Reynolds number S. $n = 1$ (–○–); $n = 2$ (–△–); $n = 3$ (–□–).

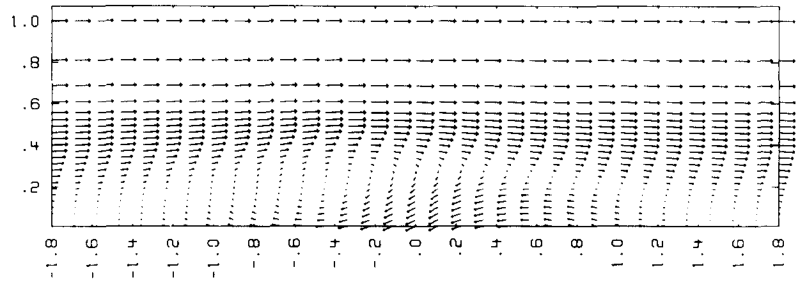

FIG. 13. FRX–B model. Superposition of perturbed poloidal field B_1 on the equilibrium poloidal field B_0; $S = 10^3$, $n = 1$. Only half the axial extent of the domain about the midplane is shown.

Although the displacement is primarily axial since $\|v_{z1}/v_{r1}\|_{\mathrm{MAX}} \sim 10$, there is flow across the axis that is aligned with the tilt.

For clarity of illustration in Figs. 13 and 14 we have displayed only half the computational domain stradling the midplane, $|z| \leqslant Z_{\mathrm{MAX}}/2$. This differs from Figs. 11 and 12 where we displayed one half plane, $0 \leqslant z \leqslant Z_{\mathrm{MAX}}$. The actual domain of computation extended for $|z| \leqslant Z_{\mathrm{MAX}}$.

The stability of nearly spherical field reversed configurations has been studied analytically by Rosenbluth and Bussac [19]. They predicted spherical configurations to be marginally stable and prolate shapes to be unstable to the $n = 1$ instability. This prediction is corroborated by the calculations of Jardin *et al.* [20] who conducted an extensive study of the tilt and shift instability of configurations resembling the spheromak. Our FRX-B simulation also agrees with theory since the theta pinch is a prolate, compact-toroidal plasma (sans toroidal field). Furthermore, nonlinear simulations by Barnes *et al.* [21] using the Lagrangian, finite-element code MALICE are in excellent agreement with our results. When both MALICE and the present program are run using similar coarse meshes, required by the 3-*D* limitation of MALICE, the growth rates agree to within 15 %. The nonlinear runs are particularly interesting as they portray the evolution of the tilting of the magnetic axis. Those

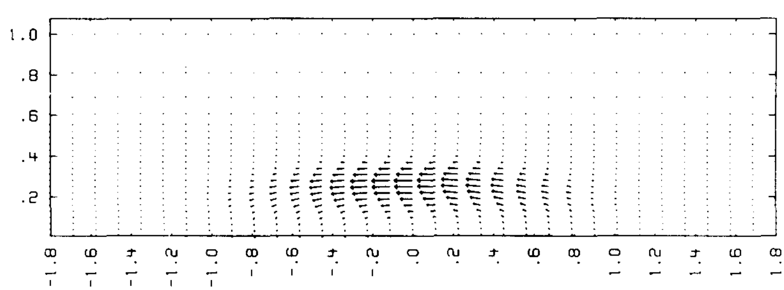

FIG. 14. FRX–B model. Perturbed velocity field; $S = 10^3$, $n = 1$.

calculations did not include effects of plasma resistivity further supporting the conclusion that our results are independent of S. Timing comparisons illustrate the usefulness of our model. The nonlinear run first required ~1 hr of CRAY − 1 computer time to "relax" the equilibrium and subsequently ~0.5 hr. for the kinetic energy to exhibit an exponential growth. An equivalent run for the program described here required 1–2 min.

In fairness we shall mention that the FRX-B experiments have been observed to possess long quiescent times in the range of 10–100 μsec before being terminated by a rotational $n=2$ instability. Furthermore, there is no evidence of tilting. We shall propose several explanations for the discrepancy. Both simulations studies of FRX-B used the equilibrium generated by Anderson and Barnes [5]. Barnes has suggested [22] that the flux surfaces of FRX may be more "ractrack shaped" rather than elliptical as in the simulations, e.g., they would closely approximate a 1-D equilibrium at the midplane. Such a configuration exhibits greater curvature of the closed magnetic contours near the ends and has the effect of "stretching" the flux surfaces. For ballooning modes ($n=\infty$), the growth rate is inversely proportional to the Alfvén transit time along the flux surface. Work is presently proceeding to determine the influence of greater "rectangularity" of these surfaces on the tilting instability. A sequence of equilibria has already been generated [23]. Secondly, our model does not include kinetic effects. In FRX, $B_{\theta 0}=0$, thus the gyroradius increases greatly near the magnetic axis. Such a process would diffuse the mode structure exerting a stabilizing influence. Furthermore FLR effects cause particles near, but inside, the separatrix to sample the field outside further restricting and diffusing the tilting motion which, in our results, is concentrated inside.

Presently the RIPPLE VI program is used to study numerically generated equilibria with toroidal field. Examples are models of the proposed Dee shaped, minor cross-section Tokamak at General Atomics Corporation in La Jolla, California. In this case the plasma region is entirely surrounded by vacuum. We set $\eta \sim p^{-3/2}$, according to classical Spitzer resistivity, since the equation of state and our incompressibility assumption imply that $p \sim T$. At the interface the diverging resistivity is smoothed into a plateau region. It is for cases where η is necessarily two dimensional that the ADI version was developed.

7. Conclusion

We have developed a numerical model applicable to the study of nonaxisymmetric instabilities of two-dimensional equilibria. The axisymmetric equilibria are given in cylindrical coordinates. Configurations of interest include both toroidal and cylindrical geometries. Typical equilibria include a plasma region surrounded by a vacuum.

We use the linearized MHD equations to obtain a system of component equations for the perturbations which are solved throughout the computational domain. Finite-difference methods are used to discretize the system and implicit methods advance the dependent variables. Although the resulting system is a coupled set of eight equations, the numerical method advances no more than two variables simultaneously. The scheme allows an iterative step which ensures convergence to second order in both space and time. In practice the iterative feature has rarely been required.

The model has corroborated earlier results and has computed the tilting mode in the reversed field theta pinch experiment. The last result has also been observed in independent nonlinear calculations which are considerably more time consuming.

APPENDIX

In this section we shall list the component equations solved by the computer program, RIPPLE VI, and describe the boundary conditions.

The relevant equations are the components of Eqs. (4) and (6). The toroidal components are eliminated using Eqs. (5) and (7); note that only the imaginary component has a superscript. We shall only give the equations for the real components (see Section 5). Equilibrium quantities are subscripted with 0, and S denotes the magnetic Reynolds number. The relevant equations are

$$\frac{\partial B_{r1}}{\partial t} = \frac{\eta}{S}\left[M(B_{r1}) + \frac{2}{r}\frac{\partial B_{z1}}{\partial z}\right] + \frac{1}{S}\frac{\partial \eta}{\partial z}\left(\frac{\partial B_{r1}}{\partial z} - \frac{\partial B_{z1}}{\partial r}\right)$$
$$+ B_{r0}\frac{\partial v_{r1}}{\partial r} + B_{z0}\frac{\partial v_{r1}}{\partial z} - v_{r1}\frac{\partial B_{r0}}{\partial r} - v_{z1}\frac{\partial B_{r0}}{\partial z} - nB_{\theta 0}\frac{v^I_{r1}}{r}, \tag{A1}$$

$$\frac{\partial B_{z1}}{\partial t} = \frac{\eta}{S}L(B_{z1}) - \frac{1}{S}\frac{\partial \eta}{\partial r}\left(\frac{\partial B_{r1}}{\partial z} - \frac{\partial B_{z1}}{\partial r}\right)$$
$$+ B_{r0}\frac{\partial v_{z1}}{\partial r} + B_{z0}\frac{\partial v_{z1}}{\partial z} - v_{r1}\frac{\partial B_{z0}}{\partial r} - v_{z1}\frac{\partial B_{z0}}{\partial z} - nB_{\theta 0}\frac{v^I_{z1}}{r}, \tag{A2}$$

$$-\frac{\partial}{\partial t}L(v_{z1}) = -\frac{\partial B_{z0}}{\partial r}\frac{\partial^2 B_{r1}}{\partial r^2} + 2\left(\frac{\partial B_{r0}}{\partial r} - \frac{B_{r0}}{r}\right)\frac{\partial^2 B_{r1}}{\partial r\,\partial z}$$
$$+ \frac{\partial B_{z0}}{\partial r}\frac{\partial^2 B_{r1}}{\partial z^2} + \left(2\frac{\partial j_{\theta 0}}{\partial r} - 2\frac{j_{\theta 0}}{r} - \frac{3}{r}\frac{\partial B_{z0}}{\partial r}\right)\frac{\partial B_{r1}}{\partial r}$$
$$+ \left(\frac{\partial^2 j_{\theta 0}}{\partial r^2} + \frac{1}{r}\frac{\partial j_{\theta 0}}{\partial r} - \frac{j_{\theta 0}}{r^2} + \frac{n^2-1}{r^2}\frac{\partial B_{z0}}{\partial r}\right)B_{r1}$$
$$- B_{r0}\frac{\partial^3 B_{z1}}{\partial r^3} - B_{z0}\frac{\partial^3 B_{z1}}{\partial r^2\,\partial z}$$
$$- B_{r0}\frac{\partial^3 B_{z1}}{\partial r\,\partial z^2} - B_{z0}\frac{\partial^3 B_{z1}}{\partial z^3}$$

$$
\begin{aligned}
&-\frac{\partial B_{r0}}{\partial r}\frac{\partial^2 B_{z1}}{\partial r^2}-\left(2\frac{\partial B_{z0}}{\partial r}+\frac{B_{z0}}{r}\right)\frac{\partial^2 B_{z1}}{\partial r\,\partial z}+\left(\frac{\partial B_{r0}}{\partial r}-\frac{B_{r0}}{r}\right)\frac{\partial^2 B_{z1}}{\partial z^2}\\
&+\left(\frac{\partial j_{\theta 0}}{\partial z}+\frac{1}{r}\frac{\partial B_{r0}}{\partial r}+\frac{n^2}{r^2}B_{r0}\right)\frac{\partial B_{z1}}{\partial r}\\
&+\left[\frac{\partial j_{\theta 0}}{\partial r}-\frac{1}{r}\left(\frac{\partial B_{r0}}{\partial z}+\frac{\partial B_{z0}}{\partial r}\right)+\frac{n^2}{r^2}B_{z0}\right]\frac{\partial B_{z1}}{\partial z}\\
&+\left(\frac{\partial^2 j_{\theta 0}}{\partial r\,\partial z}+\frac{1}{r}\frac{\partial j_{\theta 0}}{\partial z}+\frac{n^2}{r^2}\frac{\partial B_{z0}}{\partial z}\right)B_{z1}\\
&+\frac{2}{n}B_{\theta 0}\frac{\partial^3 B^I_{r1}}{\partial r^2\partial z}+\frac{2}{n}\frac{\partial B_{\theta 0}}{\partial r}\frac{\partial^2 B^I_{r1}}{\partial r^2}\\
&+\frac{2}{n}\left(\frac{\partial B_{\theta 0}}{\partial r}+\frac{2B_{\theta 0}}{r}\right)\frac{\partial^2 B^I_{r1}}{\partial r\,\partial z}+\frac{2}{n}\left(\frac{\partial^2 B_{\theta 0}}{\partial r\,\partial z}+\frac{2}{r}\frac{\partial B_{\theta 0}}{\partial z}\right)\frac{\partial B^I_{r1}}{\partial r}\\
&-\frac{2(n-1/n)}{r}\frac{\partial B_{\theta 0}}{\partial r}\frac{\partial B^I_{r1}}{\partial r\,\partial z}-\frac{2(n-1/n)}{r}\frac{\partial^2 B_{\theta 0}}{\partial r\,\partial z}B^I_{r1}\\
&+\frac{2}{n}B_{\theta 0}\frac{\partial^3 B^I_{z1}}{\partial r\,\partial z^2}+\frac{n}{r}B_{\theta 0}\frac{\partial^2 B^I_{z1}}{\partial r^2}+\frac{2}{n}\frac{\partial B_{\theta 0}}{\partial z}\frac{\partial^2 B^I_{z1}}{\partial r\,\partial z}\\
&+\left[\frac{2}{n}\frac{\partial B_{\theta 0}}{\partial r}+\frac{1}{r}\left(\frac{2}{n}+n\right)B_{\theta 0}\right]\frac{\partial^2 B^I_{z1}}{\partial z^2}\\
&+\left(\frac{2n}{r}\frac{\partial B_{\theta 0}}{\partial r}-\frac{n}{r^2}B_{\theta 0}\right)\frac{\partial B^I_{z1}}{\partial r}+\frac{2}{n}\left(\frac{\partial^2 B_{\theta 0}}{\partial r\,\partial z}+\frac{1}{r}\frac{\partial B_{\theta 0}}{\partial z}\right)\frac{\partial B^I_{z1}}{\partial z}\\
&+\left[\frac{n}{r}\frac{\partial^2 B_{\theta 0}}{\partial r^2}-\frac{n}{r^2}\frac{\partial B_{\theta 0}}{\partial r}-\frac{n}{r}\frac{\partial^2 B_{\theta 0}}{\partial z^2}-\frac{n}{r^3}(n^2-1)B_{\theta 0}\right]B^I_{z1}
\end{aligned}
\tag{A3}
$$

and

$$
\begin{aligned}
&-\frac{\partial}{\partial t}\left[M(v_{r1})+\frac{2}{r}\frac{\partial v_{z1}}{\partial z}\right]\\
&\quad=-B_{r0}\frac{\partial^3 B_{r1}}{\partial r^3}-B_{z0}\frac{\partial^3 B_{r1}}{\partial r^2\,\partial z}-B_{r0}\frac{\partial^3 B_{r1}}{\partial r\,\partial z^2}-B_{z0}\frac{\partial^3 B_{r1}}{\partial z^3}\\
&\quad-\left(\frac{\partial B_{r0}}{\partial r}+\frac{5B_{r0}}{r}\right)\frac{\partial^2 B_{r1}}{\partial r^2}-\left(2\frac{\partial B_{r0}}{\partial z}+\frac{3B_{z0}}{r}\right)\frac{\partial^2 B_{r1}}{\partial r\,\partial z}\\
&\quad+\left(\frac{B_{r0}}{r}-\frac{\partial B_{z0}}{\partial z}\right)\frac{\partial^2 B_{r1}}{\partial z^2}\\
&\quad+\left(-\frac{\partial j_{\theta 0}}{\partial z}+\frac{3}{r}\frac{\partial B_{z0}}{\partial z}+\frac{n^2-1}{r^2}B_{r0}\right)\frac{\partial B_{r1}}{\partial r}
\end{aligned}
$$

$$
\begin{aligned}
&+\left(-\frac{\partial j_{\theta 0}}{\partial r}+\frac{j_{\theta 0}}{r}+\frac{n^2-1}{r^2}B_{z0}\right)\frac{\partial B_{r1}}{\partial z} \\
&+\left(-\frac{\partial^2 j_{\theta 0}}{\partial r\,\partial z}+\frac{n^2-1}{r^2}\frac{\partial B_{r0}}{\partial r}\right)B_{r1}+\frac{\partial B_{r0}}{\partial z}\frac{\partial^2 B_{z1}}{\partial r^2} \\
&+\left(-\frac{4B_{r0}}{r}+2\frac{\partial B_{z0}}{\partial z}\right)\frac{\partial^2 B_{z1}}{\partial r\,\partial z}-\left(\frac{\partial B_{r0}}{\partial z}+\frac{2B_{z0}}{r}\right)\frac{\partial^2 B_{z1}}{\partial z^2} \\
&-\frac{1}{r}\frac{\partial B_{r0}}{\partial z}\frac{\partial B_{z1}}{\partial r}+\left(-\frac{2\partial j_{\theta 0}}{\partial z}+\frac{2}{r}\frac{\partial B_{z0}}{\partial z}\right)\frac{\partial B_{z1}}{\partial z} \\
&+\left(-\frac{\partial^2 j_{\theta 0}}{\partial z^2}+\frac{n^2}{r^2}\frac{\partial B_{r0}}{\partial z}\right)B_{z1} \\
&-\frac{2B_{\theta 0}}{n}\frac{\partial^3 B^I_{r1}}{\partial r\,\partial z^2}+\frac{n}{r}B_{\theta 0}\frac{\partial^2 B^I_{r1}}{\partial r^2}-\frac{4}{n}\frac{\partial B_{\theta 0}}{\partial z}\frac{\partial^2 B^I_{r1}}{\partial r\,\partial z} \\
&+\frac{(n-2/n)}{r}B_{\theta 0}\frac{\partial^2 B^I_{r1}}{\partial z^2}+\left(-\frac{2}{n}\frac{\partial^2 B_{\theta 0}}{\partial z^2}+\frac{3n}{r^2}B_{\theta 0}\right)\frac{\partial B^I_{r1}}{\partial r} \\
&+\frac{2}{r}(n-2/n)\frac{\partial B_{\theta 0}}{\partial z}\frac{\partial B^I_{r1}}{\partial z} \\
&+\left[-\frac{n}{r}\frac{\partial^2 B_{\theta 0}}{\partial r^2}+\frac{(n-2/n)}{r}\frac{\partial^2 B_{\theta 0}}{\partial z^2}-\frac{n}{r^2}\frac{\partial B_{\theta 0}}{\partial r}\right. \\
&\left.+\frac{n(2-n^2)}{r^3}B_{\theta 0}\right]B^I_{r1}-\frac{2B_{\theta 0}}{n}\frac{\partial^3 B^I_{z1}}{\partial z^3}-\frac{4}{n}\frac{\partial B_{\theta 0}}{\partial z}\frac{\partial^2 B^I_{z1}}{\partial z^2} \\
&-\frac{2n}{r}\frac{\partial B_{\theta 0}}{\partial z}\frac{\partial B^I_{z1}}{\partial r}+\left(-\frac{2}{n}\frac{\partial^2 B_{\theta 0}}{\partial z^2}+\frac{4n}{r^2}B_{\theta 0}\right)\frac{\partial B^I_{z1}}{\partial z} \\
&-\frac{2n}{r}\frac{\partial^2 B_{\theta 0}}{\partial r\,\partial z}B^I_{z1},
\end{aligned}
\tag{A4}
$$

where

$$
j_{\theta 0}=\frac{\partial B_{r0}}{\partial z}-\frac{\partial B_{z0}}{\partial r},
$$

$$
L(u)=\frac{1}{r}\frac{\partial}{\partial r}\left(r\frac{\partial u}{\partial r}\right)+\frac{\partial^2 u}{\partial z^2}-\frac{n^2}{r^2}u,
$$

and

$$
M(u)=L(u)+\frac{2}{r}\frac{\partial u}{\partial r}+\frac{u}{r^2}.
$$

REFERENCES

1. H. P. FURTH, J. KILLEEN, AND M. N. ROSENBLUTH, *Phys. Fluids* **6** (1963), 459.
2. J. KILLEEN, *in* "Physics of Hot Plasmas" (B. J. Rye and J. C. Taylor, Eds.), p. 202, Plenum, New York, 1970.
3. J. A. DIBIASE AND J. KILLEEN, *J. Comput. Phys.* **24** (2) (1977), 158.
4. J. KILLEEN, D. D. SCHNACK, AND A. I. SHESTAKOV, in "Computing Methods in Applied Sciences and Engineering" (R. GLOWINSKI AND J. L. LIONS, Eds.), p. 305, North-Holland, Amsterdam, 1980.
5. D. V. ANDERSON AND D. C. BARNES, *J. Comput. Phys.* **42** (1981), 288.
6. R. K. LINFORD, *et al.*, "Proceedings, 7th International Conference on Plasma Physics and Controlled Nuclear Fusion Research," 1978, IAEA, Vienna 1979, II, 447.
7. B. L. BUZBEE, G. H. GOLUB, AND C. W. NIELSON, *SIAM J. Numer. Anal.* **7** (4) (1970), 627.
8. U. SCHUMANN AND R. A. SWEET, *J. Comput. Phys.* **20** (1976), 171.
9. M. G. MCCOY, A. A. MIRIN, AND J. KILLEEN, *Comp. Phys. Comm.* **24** (1981), 37.
10. O. BUNEMAN, *J. Comput. Phys.* **29** (1978), 295.
11. J. A. DIBIASE, "Numerical Studies of Resistive Instabilities in Diffuse Pinches," Lawrence Livermore Laboratory Report UCRL-51591, May 1974.
12. A. LAPIDUS, *J. Comput. Phys.* **2** (1967), 154.
13. A. A. MIRIN, private communication, 1981.
14. S. LUNDQUIST, *Phys. Rev.* **83** (1951), 307.
15. J. KILLEEN AND A. I. SHESTAKOV, *Phys. Fluids* **21** (10) (1978).
16. H. P. FURTH, P. H. RUTHERFORD, AND H. SELBERG, *Phys. Fluids* **16** (7) (1973), 1054.
17. B. MCNAMARA *in* "Methods in Computational Physics," Vol. 16, p. 211, Academic Press, New York, 1976.
18. D. V. ANDERSON, "The Three-Dimensional Tensor Product Spline Interpolation Code (TPSIC)," Lawrence Livermore Laboratory Report UCRL-51958, 1976.
19. M. N. ROSENBLUTH AND M. N. BUSSAC, *Nucl. Fusion* **19** (4)(1979), 489.
20. S. C. JARDIN, M. S. CHANCE, R. L. DEWAR, R. C. GRIMM, AND D. A. MONTICELLO, *Nucl. Fusion* **21** (9) (1981).
21. D. C. BARNES, A. Y. AYDEMIR, D. V. ANDERSON, A. I. SHESTAKOV, AND D. D. SCHNACK, *in* "Proceedings 3rd Symposium on Physics and Technology of Compact Toroids in the Magnetic Fusion Energy Program," December 2–4, 1980, Los Alamos Scientific Laboratory, New Mexico.
22. D. C. BARNES, private communication, 1980.
23. D. V. ANDERSON AND J. M. HAMMER, *in* "Annual Controlled Fusion Theory Conference," poster 2C11, April 8–10, 1981, Austin, Texas.